Thermochimica Acta 652 (2017) 39–52

Contents lists available at ScienceDirect

Thermochimica Acta

journal homepage: www.elsevier.com/locate/tca

A new numerical method and modified apparatus for the simultaneous evaluation of thermo-physical properties above 1500 K: A case study on isostatically pressed graphite

T. Pavlov[a,b], L. Vlahovic[a], D. Staicu[a], R.J.M. Konings[a], M.R. Wenman[b], P. Van Uffelen[a,*], R.W. Grimes[b]

[a] European Commission, Joint Research Centre, Institute for Transuranium Elements, P.O. Box 2340, 76125 Karlsruhe, Germany
[b] Centre for Nuclear Engineering, Imperial College London, Royal School of Mines, London, SW7 2AZ, England, United Kingdom

ARTICLE INFO

Article history:
Received 15 July 2016
Received in revised form 27 February 2017
Accepted 7 March 2017
Available online 10 March 2017

Keywords:
Thermal conductivity
Specific heat
Laser flash
Isotropic graphite

ABSTRACT

This paper presents a new numerical inverse method coupled with an improved apparatus based on the laser flash (LF) technique for the measurement of thermo-physical properties of materials at high temperatures. Using this thermal conductivity, specific heat capacity, thermal diffusivity and spectral emissivity have been measured at temperatures above 1500 K. The method improves the characterization of input parameters such as laser power profile, which was shown to impact thermal conductivity and specific heat capacity by 15–20%. Convective heat losses are characterized semi-empirically and are not fitted. The apparatus has been enhanced via the adoption of a spectropyrometer for the simultaneous measurement of spectral emissivity within an uncertainty of 5% (equivalent to 0.3–0.7% error in temperature in the range 1500–3000 K)

The results obtained on isotropic, isostatically pressed, graphite are in good agreement with literature values (around 1500 K) and extend the available data up to 2800 K. Additionally, a model has been developed based on the theory of Debye and Klemens for predicting the temperature dependence of thermal conductivity, specific heat capacity and thermal diffusivity of isotropic graphite. The model is in good agreement with the new experimental data and previous lower temperature data and therefore provides confidence in the new experimental approach.

© 2017 The Authors. Published by Elsevier B.V. This is an open access article under the CC BY license (http://creativecommons.org/licenses/by/4.0/).

1. Introduction

The determination of thermo-physical properties of refractory materials has become crucial in tailoring the performance of machine and equipment components subjected to extreme temperatures. These properties include thermal conductivity, specific heat capacity, thermal diffusivity and emissivity and few techniques exist that facilitate measurements at high temperatures. This can be seen from Table 1, a summary of the available techniques for the measurement of properties and their practical limits. (It must be noted that the application limits presented in Table 1 are semi-quantitative and could vary from set-up to set-up. Hence the summary presented in Table 1 is indicative and helps situating the current work.)

Below 2300 K techniques such as guarded hot plate (GHP) [1], the hot wire method (HW) [2] and the radial method (RM) [3] can measure thermal conductivity relatively accurately (<10%). Differential scanning calorimetry (DSC) [4] and adiabatic calorimetry (AC) [5,6] provide accurate specific heat capacity measurements below 1900 K. The direct electrical heating (DEH) [7] method facilitates measurement of both thermal conductivity and specific heat capacity of metals up to around 3000 K, however, it is not applicable to wide band gap semi-conductors or insulators. Existing techniques for the measurement of thermal diffusivity (wave method – WM [8], and laser flash – LF[9]) have generally no equipment related, high temperature limit when heating up the sample via a laser. However, only the laser flash method has been tested at high temperatures (>2000 K). Most of the techniques for measuring emissivity (laser polarimetry – LP [10], integrating sphere reflectometry – ISR [11], multi-wavelength pyrometry – MWP [12]) have no intrinsic temperature limit since a laser can be employed to heat the sample.

* Corresponding author.
E-mail address: Paul.VAN-UFFELEN@ec.europa.eu (P. Van Uffelen).

http://dx.doi.org/10.1016/j.tca.2017.03.004
0040-6031/© 2017 The Authors. Published by Elsevier B.V. This is an open access article under the CC BY license (http://creativecommons.org/licenses/by/4.0/).

Table 1
Comparison of the different techniques for measuring thermo-physical properties. GHP- guarded hot plate; HW- hot wire; RM- radial method; DEH – direct electrical heating; AC- adiabatic calorimetry; DC- drop calorimetry; DSC- differential scanning calorimetry; LF- laser flash; WM- wave method; LP- laser polarimetry; BBC- black body cavity; ISR- integrating sphere reflectometry; MWP – multi-wavelength pyrometry; CM – comparative method. N/L stands for no limit.

	Technique					Approximate application limits				
		insulators	metals	gases	liquids	max. measurement temperature (K)	min. measurement time (s)	min. specimen size (m^3)	error range (%)	reference
Thermal conductivity	GHP	√	√	X	X	1000	5.00E + 03	4.00E – 02	0.2–4	[1,20,21]
	HW	√	X	√	√	1800	3.00E + 02	1.00E – 03	1–8	[2,3,22,23]
	RM	√	√	X	X	1800	1.00E + 03	1.00E – 03	2–12	[3,24,25]
	DEH	X	√	X	X	3000	1.00E – 01	2.00E – 06	4–14	[7,26–29]
Specific heat capacity	AC	√	√	√	√	800	2.00E + 03	7.00E – 05	0.1–2	[5,6,30,31]
	DC	√	√	X	√	3000	1.00E + 03	7.00E – 08	2–14	[32–37]
	DSC	√	√	X	√	1900	1.00E + 03	7.00E – 08	2–10	[4,38–41]
	DEH	X	√	X	√	3000	1.00E – 01	2.00E – 06	5–10	[42–44]
Thermal diffusivity	LF	√	√	X	√	N/L	1.00E – 01	2.00E – 08	2–10	[16,17,45–48]
	WM	√	√	√	√	N/L	2.00E – 01	2.00E – 08	2–10	[8,49–52]
Emissivity	LP	√	√	X	√	N/L	1.00E – 08	1.00E – 08	2–8	[29,53,54]
	BBC	X	√	X	X	3000	1.00E – 08	1.00E – 08	1–2	[54]
	ISR	√	√	X	√	N/L	1.00E – 08	1.00E – 08	1–5	[11,55–57]
	MWP	√	√	X	√	N/L	1.00E – 08	1.00E – 08	5–15	[12,58]
	CM	√	√	√	√	2000	1.00E – 08	1.00E – 08	1–2	[41,59]

It is evident that few techniques are applicable at temperatures above 2000 K and even fewer that exceed 3000 K. The summary in Table 1 suggests that the LF technique is a strong candidate for the measurement of high temperature thermo-physical properties. In addition LF also offers other significant benefits: 1) very short measurement time and thus limits possible sample instability – vaporisation, dissociation, etc.; 2) relatively small sample size; 3) wide applicability to conductive and non-conductive solids. The current study will also utilize another advantage of the LF technique: the possibility of simultaneously determining specific heat, thermal diffusivity and thermal conductivity. These make the LF method well suited for testing nuclear fuel materials at temperatures representative of reactor accident conditions [13]. In particular the LF method can be used on a single specimen to obtain multiple thermo- physical properties, which can be very beneficial in the case of limited availability and quantity of irradiated nuclear materials. Also, the technique can be particularly suitable for examining aerospace materials at elevated temperatures (e.g. the temperatures experienced by thermal protection systems during hypersonic flight [14,15]).

In the LF technique (initially developed by Parker [9]) an energy pulse is supplied to one side of a sample and the thermal response (temperature elevation as a function of time) is measured on the other side [9]. Parker's solution assumes: a) an instantaneous surface heat source; b) opaque sample; c) no heat losses and d) axial heat flow. Other analytical solutions were introduced to better describe heat losses [16], allowing for the technique to be applied at higher temperatures. Ronchi et al. [17] and Baba et al. [18] introduced an optical fibre in order to homogenise the spatial profile of the laser beam, while Ronchi et al. [17] also considered both radial and axial heat flow in their analytical solution of the heat equation and attempted to simultaneously determine specific heat capacity, thermal diffusivity and conductivity. However, Ronchi et al. used the heat transfer coefficient, emissivity and laser beam radius as possible fitting parameters, which they showed could lead to overfitting [17]. Furthermore, it was assumed that the spatial profile of the laser can be represented by a top hat function, and whilst this is a good approximation and can be very representative in some more high quality laser flash units [18,19], it is not exact and can lead to significant uncertainties in lower quality LF setups.

In the context of increasing needs for facilities and techniques capable of measuring thermal conductivity, specific heat capacity, thermal diffusivity and emissivity at high temperatures, the present study will utilizea LF-MWP apparatus coupled with a novel numerical model for the determination of these properties. The new inverse method, in addition to having the previously described LF features, also accurately describes the spatial power profile of the laser and the impact of this on evaluating specific heat capacity and thermal conductivity. This enables the method to be used with lasers, which may have a spatial profile deviating from the perfect top hat shape. Furthermore, convective heat losses are characterized semi-empirically rather than fitted. Spectral emissivity is simultaneously measured via the MWP method as part of the same experiment, facilitating an accurate conversion from radiance to true temperature.

The new method was applied to isotropic isostatically pressed graphite and extends the available literature data up to 2800 K. Furthermore, the experimental data will be supported by a solid state physics model with the purpose of describing the governing physical phenomena responsible for the evolution of the properties with temperature. The potential agreement between model and experiment will provide more confidence in the proposed methodology and associated high temperature experimental results.

2. Methodology

2.1. Experimental methodology

A schematic of the LF experiment and related equipment is shown in Fig. 1. The apparatus includes a disc shaped sample, held by three or four zirconia pins to a graphite sample holder, all of which are sealed within a chamber. The sample can have a diameter between 5 and 12 mm and the thickness tends to be in the range of 0.5–3 mm. In this work two nearly identical graphite samples were used with a thickness of around 3 mm and diameter of 4.95 mm. The dimensions of the samples were measured using a thickness gauge and Vernier Callipers. The weight of the samples was measured using an analytical balance. From the measured dimensions and respective weights of the cylindrical samples, the room temperature density was calculated. The specimens are kept under a controlled atmosphere. The pressure in the

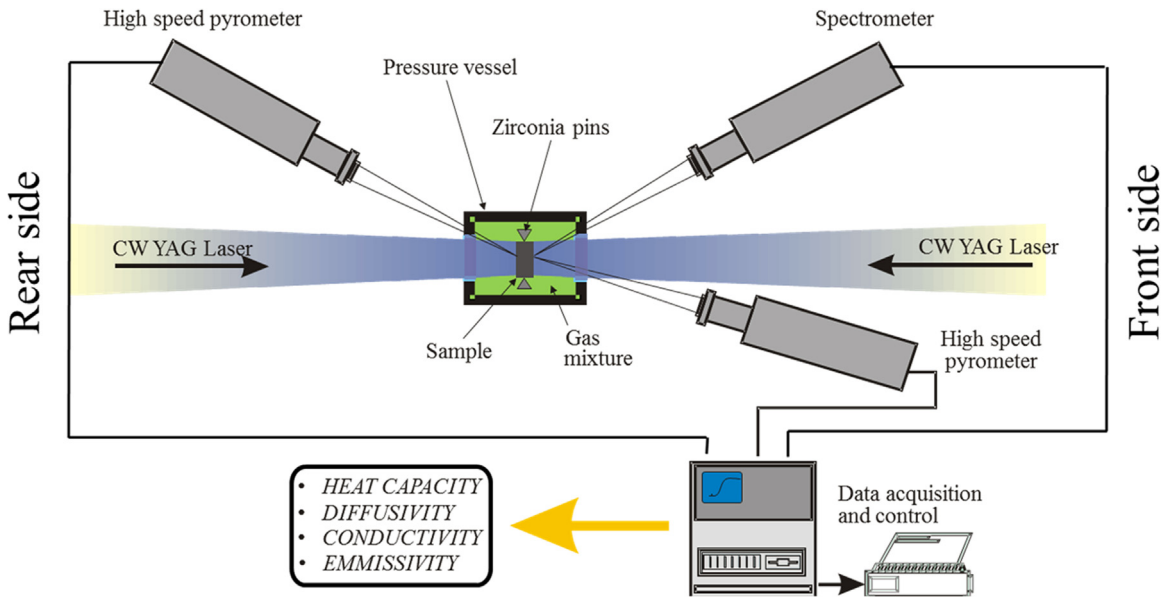


Fig. 1. Schematic of the laser flash experimental set-up.

chamber can be varied between 5 μbar and 4 bar (possible buffer gases include: argon, oxygen, argon/hydrogen, air, carbon dioxide). For all current measurements argon was used as a buffer gas. There are transparent sapphire windows on both sides of the stainless steel chamber, which allow for two continuous-wave lasers (Nd-YAG with λ = 1064 nm), to preheat each side of the specimen from around 300 K to a chosen equilibrium temperature. The equilibrium temperatures can be varied from around 1000 K to above 3000 K. The temperatures are continuously monitored by high speed pyrometers on the front and rear sides. Furthermore, a spectropyrometer measures the radiance on the front side at 256 wavelengths in the range 500 nm–1000 nm. The spectropyrometer has a nominal spot diameter of 0.4 mm and a maximum deviation from linearity of 0.3% of end point. The pyrometers as well as spectropyrometer have been calibrated using both tungsten ribbon lamps and a black body.

Once the desired steady-state temperature has been reached (the temperature measured by the pyrometer becomes stable over time) a short pulse is applied (generally around 10 ms) using the front Nd-YAG laser. On the rear side, the rise in temperature is measured as a function of time via a pyrometer, which is automatically triggered upon the initiation of the laser pulse. The pyrometer measurements are transferred to a 14-bit digitiser (Nicolet Pro 34) and subsequently the radiance signal is converted into temperature.

The samples are made out of polycrystalline graphite produced by cold isostatic pressing. The specimens were produced by SLG carbon group and are grade R6650P5 with purity above 99.9998%.

2.2. Computational methodology

A logic diagram of the method is shown in Fig. 2. The experimental thermograms are converted from a signal reading to a temperature reading. Prior to the onset of the pulse the temperature is recorded, which provides the information necessary for a base line correction. Furthermore, Fast Fourier transforms are employed to filter high frequency noise.

2.2.1. Noise filtering

In order to filter the inherent data noise, fast Fourier transforms (FFT) were employed. A low frequency band pass filter was used, cutting off high frequency noise. The cut-off frequency was chosen such that the accuracy of the fitted parameters was not affected. This has been tested using synthetic thermograms with known properties, which were passed through filters of different band width. The narrowest band width, which did not hinder the accuracy, was chosen and corresponds to 1–200 kHz (2% of the total frequency spectrum) and hence 98% of the high frequencies are filtered.

2.2.2. Finite Element Analysis (FEA)

The FEA model, which has been created with the FlexPDE [60] software, is axisymmetric (shown in Fig. 3). The model describes the onset of the transient conditions in the sample immediately after the application of the laser pulse.

The governing equation is the transient heat equation:

$$\rho c_p \frac{\partial T}{\partial t} = \nabla \cdot (k \nabla T) + q \quad (1)$$

where q is the volumetric heat source ($J\,s^{-1}\,m^{-3}$), ρ is the density ($kg\,m^{-3}$), c_p is the specific heat capacity at constant pressure ($J\,kg^{-1}\,K^{-1}$)), k is thermal conductivity ($J\,s^{-1}\,m^{-1}\,K^{-1}$), T is temperature (K) and t is time (s).

In this case there is no volumetric heat source (q = 0). Furthermore, a reduced variable is introduced such that:

$$T(t, r, z) = T(0, r, z) + \Psi(t, r, z) = T_0 + \Psi \quad (2)$$

where T_0 is the steady state temperature (K) and Ψ is the reduced variable temperature (K). Hence, the reduced boundary conditions are:

$$k \frac{\partial \Psi}{\partial z}\Big|_{z=0} = \theta(r, t) \times \varepsilon_{1064} - h(T) \times [T - T_0] - \varepsilon_{tot}(T) \times \sigma \times \left[T^4 - {T_0}^4\right] \quad (3)$$

$$k \frac{\partial \Psi}{\partial z}\Big|_{z=t_{sample}} = -h(T) \times [T - T_0] - \varepsilon_{tot}(T) \times \sigma \times \left[T^4 - {T_0}^4\right] \quad (4)$$

$$k \frac{\partial \Psi}{\partial r}\Big|_{r=r_{sample}} = -h(T) \times [T - T_0] - \varepsilon_{tot}(T) \times \sigma \times \left[T^4 - {T_0}^4\right] \quad (5)$$

where *h(T)* is the temperature dependent convective heat transfer coefficient ($W\,m^{-2}\,K^{-1}$), ϵ_{tot} is the total hemispherical emissivity and $\epsilon_{(1064nm)}$ is the emissivity at the laser wavelength (absorptivity).

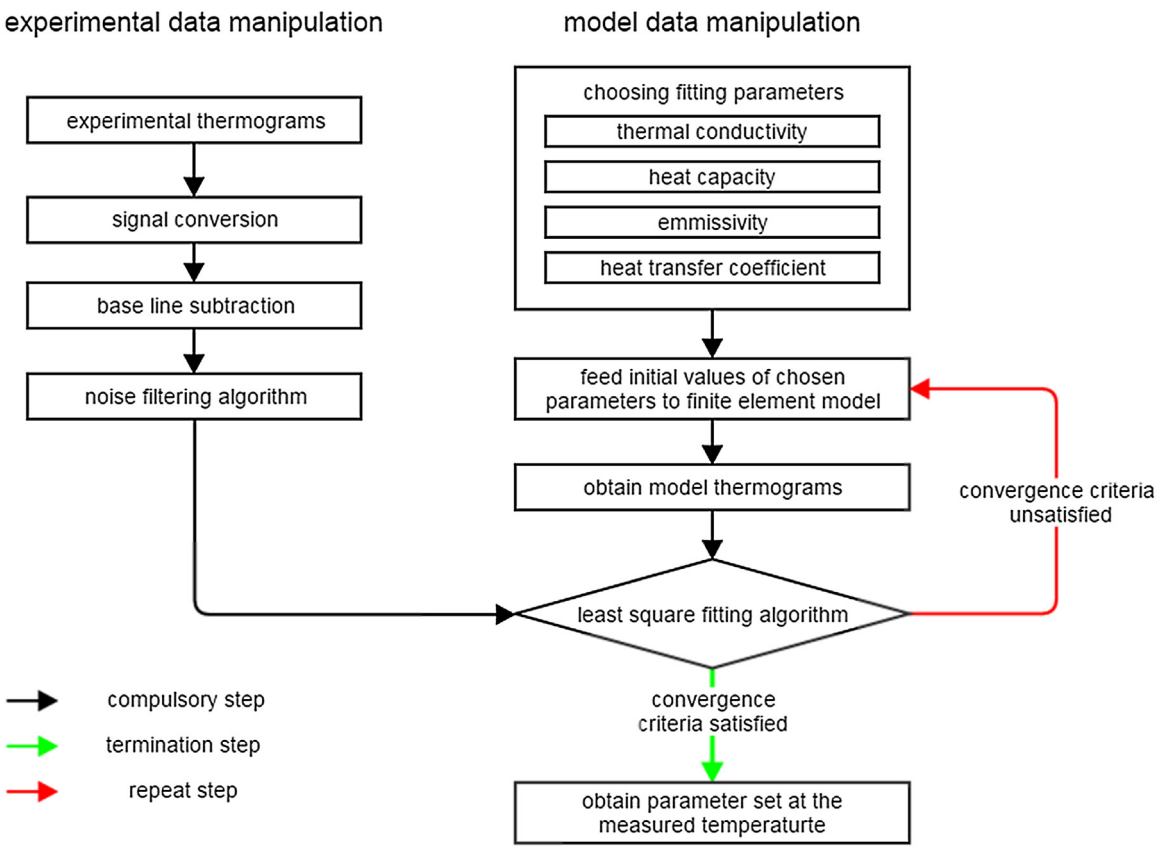


Fig. 2. Logic scheme of computer programme.

The initial condition is:

$$\Psi_{t=0} = 0 \tag{6}$$

The properties of the graphite samples used are tabulated in Table 2 while the FEA mesh is displayed in Fig. 3. Quadratic triangular elements (6 nodes per element) have been used. Adaptive re-meshing has been used in order to achieve convergence on the temperature output of the model to less than 0.001 K. Furthermore, the model is based on the approximation of an isothermal steady state, which was tested using synthetic (calculated) thermograms and was shown to hold within an accuracy of less than 1% of the fitted properties. Furthermore, the effect of the zirconia pins was examined (via a full 3-D FEA model) and found negligible due to the low thermal conductivity of zirconia and the small contact area with the sample.

The power profile of the laser is time and space dependent. The time dependence of the power is measured by a voltmeter (voltage is converted to power based on a calibration curve) and can be accurately described by a top hat function for pulses longer than 5 ms. The spatial profile has been measured and calibrated using a USBeamPro PS-2323 beam profiler. The spatial profile has been calibrated for powers of 50 W and 100 W and the best focus has been determined invariant within a range of 14 mm. Furthermore, measurements of the defocused profile were performed up to 60 mm away from the best focus, in order to set conservative limits for the error analysis (50 mm defocusing). The spatial profile of the laser can be described via two intersecting linear functions (shown in Fig. 6 and Eq. (11)). The space-time profile, described by the $\theta(r, t)$ function in Eq. (3), can be expanded in the following manner:

$$\theta(r, t) = \frac{P(r, t)}{\pi {r_b}^2} = \frac{P(r) \times P(t)}{\pi {r_b}^2} \tag{7}$$

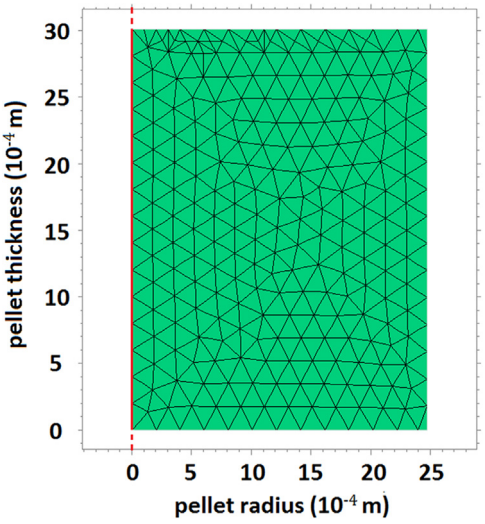


Fig. 3. The geometry of the axisymmetric model and the mesh used in FlexPDE. The red dashed line denotes the axis of symmetry at r = 0. (For interpretation of the references to colour in this figure legend, the reader is referred to the web version of this article.)

where $P(\mathrm{J\,s^{-1}})$ is the power of the laser pulse, θ is the power density ($\mathrm{J\,s^{-1}\,m^{-2}}$) deposited by the beam, r_b is the nominal beam spot radius (m).

2.2.3. Optimization algorithm

The Levenberg-Marquardt method [63,64] was used to find the least squares minimum between the experimental thermograms and the model thermograms. The convergence criteria used is the

Table 2
Material properties and sample dimensions of isostatically pressed graphite. (density (ρ_{298}), thickness (t_{sample}), radius (r_{sample}) measured at temperature T = 298 K and pressure p = 0.1 MPa; average spectral emissivity at 640 nm ($\epsilon_{(640nm)}$) in the temperature range 1700–2400 K measured at pressure p = 0.4 MPa).

Material properties (isostatically pressed graphite)		Reference
RT density ρ_{298} (kg m^{-3})	1804	measured (this work)
$\rho(T)^{+}$	$\rho_{298} \times \left(\begin{matrix} -1.174 \times 10^{-12} T^3 + 1.677 \times 10^{-5} T^2 - \\ -1.676 \times 10^{-5} T + 1.005 \end{matrix} \right)$	Hay et al. [61]
$\epsilon_{(1064nm)}{}^{+}$	$4.053 \times 10^{-5} T + 0.874$	Hay et al. [61]
$\epsilon_{(640nm)}$	0.87	measured (this work)
$\epsilon_{tot}{}^{+}$	$0.92 - 5.33 \times 10^{-5} T$	Matsumoto et al. [62]
Sample dimensions		
Thickness t_{sample} (mm)	3.03	measured (this work)
Radius r_{sample} (mm)	2.475	measured (this work)
Laser beam characteristics		
beam spot radius r_b (mm)	1.5	measured (this work)
Pulse duration (ms)	10	measured (this work)

[+] polynomial fits to experimental data obtained from the respective reference
[a] Standard uncertainties u(p) = 4 kPa, u(T) = 2 K, u(ρ_{298}) = 5 kg m^{-3}, u(t_{sample}) = 0.005 mm, u(r_{sample}) = 0.005 mm, u($\epsilon_{(640nm)}$) = 0.05.

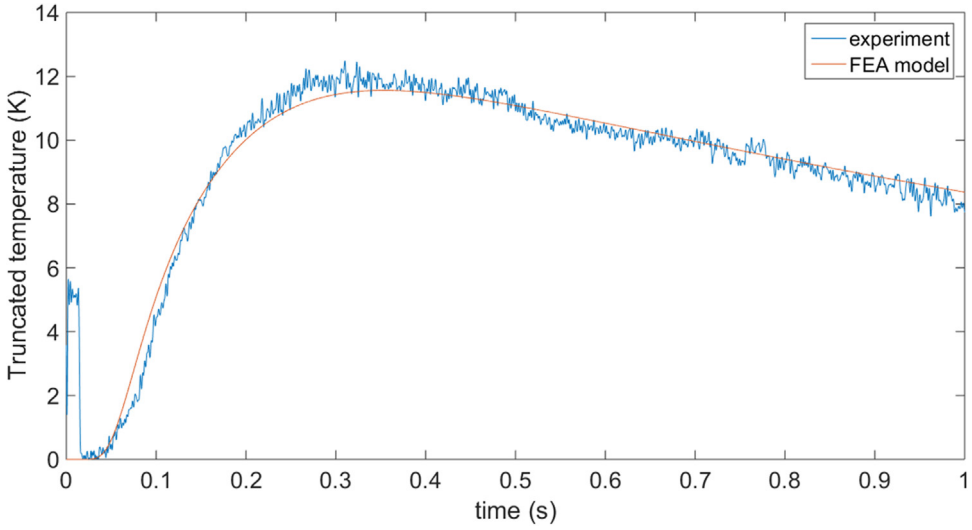


Fig. 4. Example of a thermogram-temperature vs. time graph obtained from experiment compared to the model thermogram obtained via least squares minimization.

relative difference in the parameter vector between two consecutive iterations. If the difference in all individual parameters was lower than 10^{-4} of the current parameter estimate, the code terminates. The fitted parameters are thermal conductivity (k) and specific heat capacity (C_p) and hence the parameter vector is:

$$p = \begin{pmatrix} k \\ c_p \end{pmatrix} \tag{8}$$

The computer code, however, has been designed in a flexible manner, whereby any combination of 4 fitting parameters (thermal conductivity (k), specific heat capacity (C_p), total hemispherical (ϵ_{tot}) and heat transfer coefficient (h)) can be chosen, while providing the other unselected parameters as input.

3. Application of method to fine grained isotropic graphite

An example thermogram is shown in Fig. 4. The thermogram's ascent is dominated by the thermal diffusivity and conductivity, the amplitude of the thermogram is predominantly dependent on the specific heat capacity and density of the material, while the descent is due to heat losses such as convective and radiative heat transfer.

3.1. Sensitivity analysis

In order to examine the relative importance of the different model parameters a sensitivity analysis was performed. The sensitivity analysis shown in Fig. 5 is based on the following numerical derivative:

$$S = p\frac{df}{dp} \tag{9}$$

where S is the sensitivity coefficient (K), p is the respective parameter, f is the temperature output of the FEA model or model thermogram (K). The parameters with the highest absolute sensitivity coefficients (positive or negative) will have the strongest effect per change in parameter on the model output thermogram. Hence, small changes in these sensitive parameters will lead to relatively big differences in the model output. Furthermore, parameters with sensitivity coefficients close to zero will have a much lower relative effect on the calculated output.

The sensitivity analysis in Fig. 5 shows that the highest absolute sensitivity was exhibited by sample thickness (t_s) at 0.12 s. However, the spatial profile shows the greatest integral sensitivity over the first 1.5 s. The spatial profile sensitivity has been obtained by changing the parameters describing the radial dependence of the power (Section 2.2.2). These are incrementally changed from values corresponding to the most focused state of the laser beam to values

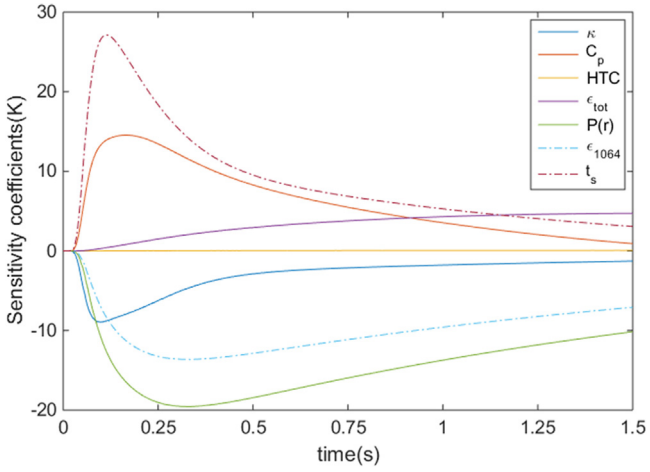


Fig. 5. Sensitivity coefficients vs. time for thermal conductivity (κ), specific heat capacity (c_p), convective heat transfer coefficient (HTC), the total hemispherical emissivity (ε_{tot}), spatial laser beam profile (P(r)), absorptivity (ε_{1064}) and thickness (t_s).

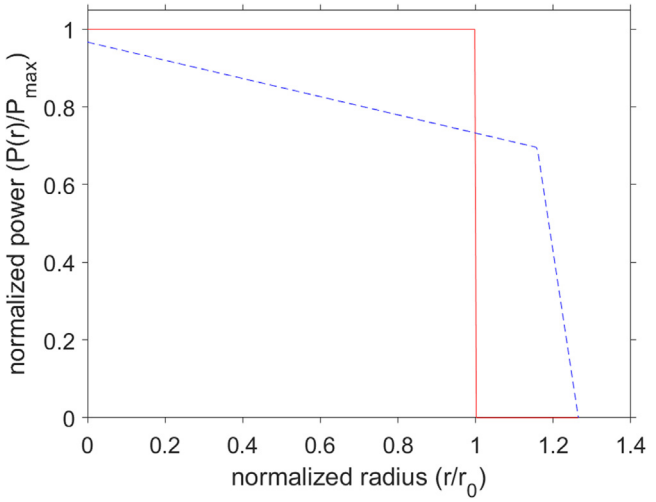


Fig. 6. The calibrated spatial profile (blue dashed line) of the laser compared to a top hat approximation of the spatial laser profile (red line). P(r) represents the calibrated or measured power as a function of radius, while P_{max} represents the integral power. (For interpretation of the references to colour in this figure legend, the reader is referred to the web version of this article.)

of a more defocused state. Furthermore, it can be concluded that the thermogram is sensitive to thermal conductivity and specific heat capacity. This is important as it shows that relatively small changes in these properties will have a measurable effect on the thermogram. Additionally, since the peaks and shapes of the curves are noticeably different, this means the two are not highly correlated. Hence, the method is suitable for the determination of these two properties by fitting. It must be noted that the sensitivity coefficient of density (ρ) follows exactly the one of specific heat capacity (c_P) and has not been plotted in Fig. 5 for better clarity. This means that these two properties are completely correlated – a result of the formulation of the heat equation (Eq. (1)) where specific heat capacity and density are the two multiples composing the energy stored per unit temperature. Furthermore, it is evident that the sensitivity coefficients of total hemispherical emissivity, spatial laser profile, absorptivity, density (equivalent to c_P) and thickness are all significant. Hence, uncertainties in these input parameters can propagate and lead to an appreciable uncertainty in the calculated output (specific heat capacity and thermal conductivity). Therefore these will be examined carefully and based upon their uncertainty, it will be possible to estimate the model output error (described in section 4.8). It is worth noting that for certain materials with poorly understood high temperature properties, such as thermal expansion and hence density, the current method would need to be coupled with techniques for measuring these properties.

3.2. Impact of the laser beam's spatial profile

From the sensitivity analysis it was shown that one of the most influential parameters was the spatial profile of the laser beam. In Fig. 6 the spatial profile (calibrated for the optical arrangement) of the laser is compared to a top hat function. The integral of the power with respect to the normalized radius is the same for both profiles. This implies that the total laser power was the same in each case, only its spatial distribution differs. It is evident that the actual characteristics of the laser beam are significantly different from the assumed top hat characteristics. Previous studies that developed similar methods have used the approximate top hat form in their analytical model (a sufficiently accurate approximation in their case considering they had measured a relatively flat near square shaped spatial power profile) and also fitted parameters such as r_0 (beam spot or waist radius) [65]. The latter may be problematic due to a high degree of correlation between the beam spot radius and specific heat. In this work the more representative spatial laser profile (for the presented optical configuration in Fig. 1) will be implemented in the finite element model. In order to examine the effect of the spatial profile on the fitted properties (thermal conductivity and specific heat), two cases will be run for a single thermogram at 1536 K. The first case will evaluate the property using the top-hat approximation as input, while in the second case the calibrated or measured profile will be used.

Table 3
A comparison between the calculated properties (thermal conductivity (k) and specific heat (c_p)) using the calibrated and top hat laser profiles at pressure p = 0.4 MPa. Furthermore, results are compared to the values obtained by Hay et al. [41].

	T (K)	k (W m^{-1} K^{-1})	c_p (J kg^{-1} K^{-1})
Top hat approximation	1536	46.93	2327
Calibrated profile	1536	40.87	1938
B. Hay et al. (JRC – ITU) [41]	1523	42.04	1976

[a]Combined expanded relative uncertainties $U_r(T) = 0.7\%$, $U_r(c_P) = 15.2\%$, $U_r(k) = 19.4\%$, $U_r(\alpha) = 15.0\%$ with 0.95 level of confidence (coverage factor of 2).

The top hat function has been implemented in the finite element model as follows:

$$P(r)\begin{cases} P_{max} for 0 \le \dfrac{r}{r_B} \le 1 \\ 0 for \dfrac{r}{r_B} > 1 \end{cases} \quad (10)$$

The calibrated profile is expressed in the following manner:

$$P(r)\begin{cases} P_{\max}\left(0.967 - 0.2342 \times \dfrac{r}{r_B}\right) for 0 \le \dfrac{r}{r_B} \le 1.1587 \\ P_{\max}\left(8.2923 - 6.5561 \times \dfrac{r}{r_B}\right) for 1.1587 \le \dfrac{r}{r_B} \le 1.2648 \\ 0 for \dfrac{r}{r_B} > 1.2648 \end{cases} \quad (11)$$

The impact of the different spatial laser profiles is presented in Table 3. It is evident that the effect on thermal conductivity and specific heat capacity is around 15% and 20% respectively. Furthermore, the values obtained via calorimetry measurements combined with conventional LF diffusivity measurements at JRC – ITU[41] were in very good agreement with the output from the method using the calibrated power profile. However, this finding does not discard

Table 4
Comparison of the effect of noise filtering on the fitted properties (thermal conductivity and specific heat capacity), the computational time (t_{comp}) and signal to noise ratio (SNR) for a thermogram at temperature T = 2219 K and pressure p = 0.4 MPa.

	T (K)	k (W m^{-1} K^{-1})	c_p (J kg^{-1} K^{-1})	SNR (10^3)	t_{comp} (10^3 s)
Unfiltered	2219	35.64	1895	1.406	2.789
Filtered	2219	35.64	1895	2.443	1.834

[a] Standard uncertainties u(p) = 4 kPa, u(SNR) = 1, u(t_{comp}) = 1 s, combined expanded relative uncertainties $U_r(T) = 0.7\%$, $U_r(c_P) = 15.2\%$, $U_r(k) = 19.4\%$, $U_r(\alpha) = 15.0\%$ with 0.95 level of confidence (coverage factor of 2).

the accuracy of studies where the laser spatial profile was square shaped, it just serves to show the numerical model can be used to harness the full potential of the LF method when using lasers with spatial power profiles deviating from the ideal.

3.3. Impact of noise filtering

The signal to noise ratio can be improved either by post-processing the experimental data by noise filtering or increasing the laser pulse power and hence increasing the signal gain. The second is appropriate only to the extent, whereby the fitted properties are not significantly impacted by the temperature variation of the sample (e.g. large temperature amplitude on the front side leading to deviation from the equilibrium assumption or inducing phase changes, such as melting). Hence, a combination of sufficient signal gain and adoption of noise filtering has been used. In Table 4 the results for thermal conductivity and specific heat capacity of isostatically pressed graphite are compared for two cases: 1) a noisy (unfiltered) thermogram; 2) the same thermogram passed through the low pass filter (filtered). The values of these two properties are exactly the same in both cases. However, the signal to noise ratio and the computation time are significantly improved when using the FFT low pass filter.

3.4. Convective heat transfer coefficient

One of the heat loss mechanisms is natural convection and is described by a convective heat transfer coefficient. Previously values for this property have been either fitted [65], arbitrarily chosen [66] or approximated as constant over a broad temperature range [67]. In this work the convective heat transfer coefficient is semi-empirically evaluated based on the sample geometry and the properties of the gaseous atmosphere. The relationship in eq. (10) has been used in order to derive the heat transfer coefficient ($\bar{h}_D$) as a function of temperature.

$$\bar{h}_D = \frac{\overline{Nu}_D k_g}{D} \tag{12}$$

where k_g represents the thermal conductivity of the gas (W m^{-1} K^{-1}), D is the sample diameter (m) and $\overline{Nu}_D$ represents the Nusselt number. Churchill and Chu [68] suggested the following expression for the Nusselt number during laminar flow for a vertical plate:

$$\overline{Nu}_D = 0.68 + 0.67 \times Ra_D{}^{1/4}\left\{1 + \left[\frac{0.492}{\mathrm{Pr}}\right]^{9/16}\right\}^{-4/9} \tag{13}$$

where Ra_D and Pr are the Rayleigh and Prandtl numbers.

$$Ra_D = \frac{g\beta\Delta T D^3}{\alpha\nu} \tag{14}$$

$$Pr = \frac{\alpha}{\nu} \tag{15}$$

where g is the gravitational acceleration (m s^{-2}), β is the gas compressibility, α is the gas thermal diffusivity (m^2 s^{-1}) and ν is the kinematic viscosity of the gas (m^2 s^{-1}). The properties of argon have been taken from Little[69] and Stewart et al. [70].

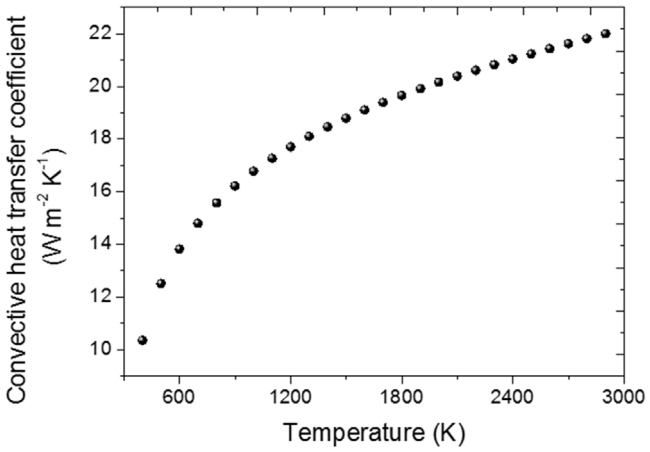


Fig. 7. Calculated heat transfer coefficient as a function of temperature at a pressure of 1 bar.

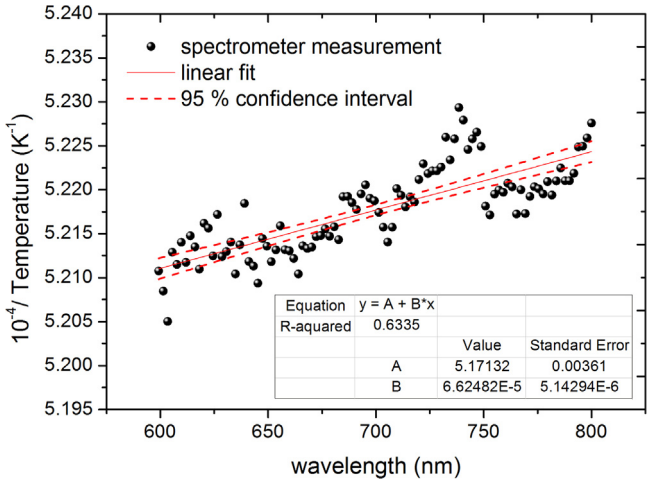


Fig. 8. Inverse temperature as a function of wavelength measured by a 256 channel spectropyrometer.

The results from Eqs. (12)–(15) for the convective heat transfer coefficient are shown in Fig. 7 and are used as input in the finite element model.

3.5. Spectral emissivity (640 nm)

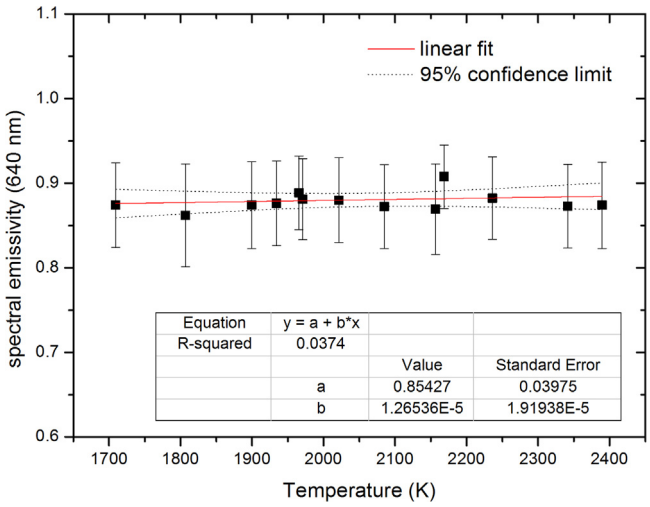
At higher temperatures (>2000 K) the uncertainty in normal spectral emissivity can lead to significant temperature measurement uncertainties.

$$\frac{1}{T_B} = \frac{1}{T_R} + \frac{\lambda}{c_2}\ln(\varepsilon) \tag{16}$$

where c_2 is the second radiation constant (m K), λ is the wavelength (m), T_R is the radiance temperature (K) and T_B is the black body temperature (K).

Eq. (16), also known as Wien's law [71] can be used to estimate the true temperature and emissivity from multi-wavelength pyrometry. Assuming that this property does not vary within a given wavelength range (600–800 nm) and from the measured radiances (and hence temperatures) at different wavelengths (via a multi-wavelength spectropyrometer) the emissivity can be retrieved from the linear fit shown in Fig. 8.

Once, the spectral emissivity at the pyrometer wavelength (shown in Fig. 8) has been determined, the pyrometer radiance



tblSpectral emissivity at a wavelength of 640 nm for fine grained polycrystalline graphite.

Table 5
Measurements of normal spectral emissivity at 640 nm ($\epsilon_{(640nm)}$) and respective uncertainties at various temperatures and at a pressure p = 0.4 MPa.

T (K)	$\epsilon_{(640nm)}$ (−)	uncertainty of $\epsilon_{(640nm)}$
1966	0.889	0.043
1971	0.881	0.048
2168	0.908	0.038
2341	0.873	0.049
2390	0.874	0.051
2236	0.882	0.049
2085	0.872	0.050
2157	0.869	0.054
2022	0.880	0.050
1934	0.876	0.050
1900	0.874	0.051
1807	0.862	0.061
1709	0.874	0.050

[a] Standard uncertainty u(p) = 4 kPa, combined expanded relative uncertainty $U_r(T) = 0.7\%$ with 0.95 level of confidence (coverage factor of 2) and expanded uncertainty $U(\epsilon_{(640nm)})$ estimated for each measurement with 0.95 level of confidence (coverage factor of 2).

temperatures (T_R) can be converted into true temperatures (T_B) again using Eq. (16).

The low R-squared value of the linear fit in Fig. 9 is due to the residual sum of squares (difference between data and fit) being comparable to the total sum of squares (difference between data and data mean). This indicates that the mean of the data is almost identical to the fitted line. Hence, the spectral emissivity at 640 nm (Table 5) can be considered temperature invariant in the range 1700 K to 2400 K. The mean value of 0.87, also shown in Table 2, will be used to convert the radiance temperature to true temperature.

In order to examine the importance and effect of emissivity the following formulation can be obtained from the derivative of emissivity with respect to true temperature:

$$dT_B = \frac{T^2 \lambda d\varepsilon}{c_2 \varepsilon} \tag{17}$$

It can, hence, be estimated that for a given uncertainty in emissivity of 30%, the uncertainty in the measured temperature at 640 nm would be 54 K at 2000 K (≈2.7%) and rising to 121 K at 3000 K (≈4%). Hence, an accurate value of normal spectral emissivity is necessary to reduce the uncertainty in the measured temperature.

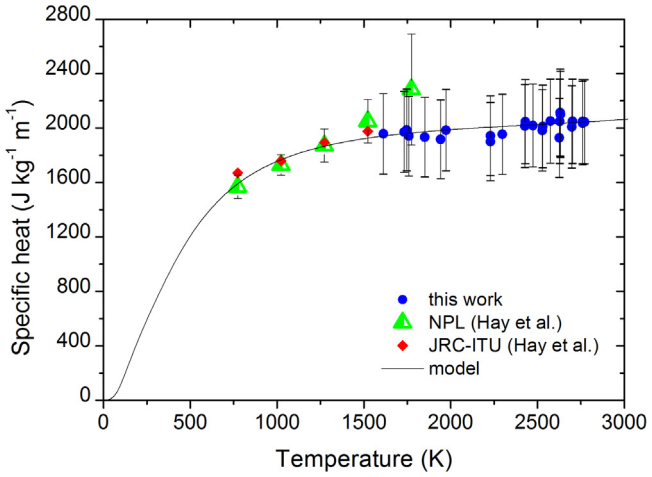


Fig. 10. Measured specific heat capacity as a function of temperature for polycrystalline graphite compared to the calculated specific heat capacity using Eq. (20). The literature data (green triangles and red rhombohedra) has been taken from Hay, et al. [61]. The error bars on the blue data points correspond to two standard deviations and are equivalent to 15.2% relative error (for details on error analysis refer to Section 4.3). (For interpretation of the references to colour in this figure legend, the reader is referred to the web version of this article.)

3.6. Specific heat capacity

Measurements of specific heat capacity, thermal conductivity and thermal diffusivity are summarised in Table 6 and presented in Figs. 10 11 and 12, respectively, where they are compared to literature data obtained from the same batch of isostatically pressed graphite.

The specific heat capacity results obtained from the inverse method, described in this work, are shown in Fig. 10. The estimated error (equivalent to two standard deviations) was 15%. It is evident that there is good agreement between the measured heat capacities and previously reported values at temperatures close to 1500 K. Around 1800 K, the results obtained in the National Physical Laboratory (NPL) by Hay et al. [61] show a steeper increase in specific heat capacity relative to the measurements in this work. In view of this discrepancy and in order to gain a physical understanding of the phenomena that govern the temperature dependent changes of this property, a physical model was developed. It is based on solid state theory and will be extended to predict thermal conductivity and hence thermal diffusivity as a function of temperature. The theory of the model will be described and discussed in Section 4.

3.7. Thermal conductivity

The estimated error on the thermal conductivity data presented in the current study is just under 20%. Fig. 11 shows that at temperatures close to 1500 K the thermal conductivity results obtained are in excellent agreement with the ones measured by Hay et al. [61]. At around 1800 K, there was some disagreement between the current results and the ones obtained at the NPL [61]. This work suggests a continued degradation of thermal conductivity with respect to temperature in the range 1500 K–1800 K, while the NPL results show that the rate of decrease in thermal conductivity with respect to temperature is more gradual. The model data is in very good agreement with most of the experimental results.

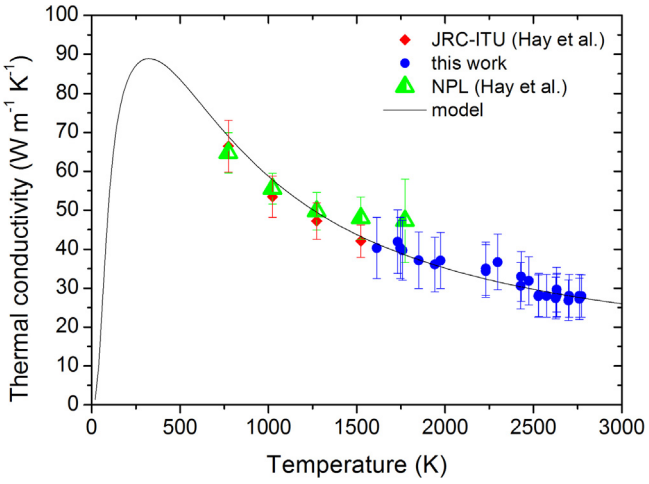


Fig. 11. Thermal conductivity of isotropic graphite as a function of temperature. Experimental data is compared to the model described in this work. The error bars on the blue data points correspond to two standard deviations and are equivalent to 19.4% relative error (for details on error analysis refer to Section 4.3). (For interpretation of the references to colour in this figure legend, the reader is referred to the web version of this article.)

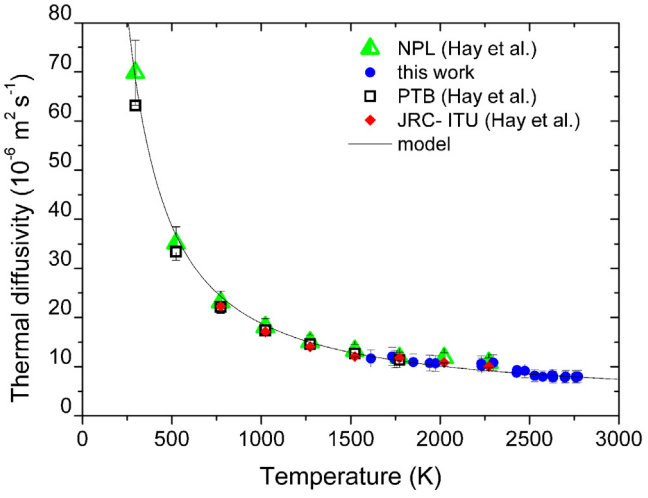


Fig. 12. Thermal diffusivity of isotropic graphite as a function of temperature. The error bars on the blue data points correspond to two standard deviations and are equivalent to 15% relative error (for details on error analysis refer to Section 4.3). (For interpretation of the references to colour in this figure legend, the reader is referred to the web version of this article.)

3.8. Thermal diffusivity

The uncertainty in thermal diffusivity was estimated to be close to 15%. The thermal diffusivity has been obtained from the specific heat capacity, thermal conductivity and density as follows:

$$\alpha(T) = \frac{k(T)}{\rho(T)\, c_p(T)} \tag{18}$$

Fig. 12 shows excellent agreement between the diffusivity obtained in this work and the results of Hay et al. [61] The model for thermal diffusivity is based on the models for specific heat capacity and thermal conductivity linked via Eq. (18) (using the measured density in this work, corrected for thermal expansion based on the work of Hay, et al. [61]). Furthermore, the model describes the temperature evolution of diffusivity almost exactly.

Table 6
Measurement values of specific heat (c_P), thermal conductivity (k) and thermal diffusivity (α) as a function of temperature at a pressure p = 0.4 MPa.[a]

T (K)	c_P (J kg^{-1} K^{-1})	k (W m^{-1} K^{-1})	α (10^{-6} m^2 s^{-1})
1613	1957	40.28	11.67
1732	1971	41.92	12.09
1747	1985	40.27	11.54
1759	1941	39.69	11.64
1850	1933	37.12	10.95
1942	1917	36.06	10.75
1974	1984	37.08	10.69
2230	1900	35.03	10.61
2232	1943	34.36	10.18
2298	1954	36.66	10.82
2428	2015	30.56	8.78
2430	2047	32.98	9.33
2474	2018	31.82	9.14
2528	1983	27.93	8.18
2531	2011	28.22	8.15
2574	2051	28.01	7.95
2574	2051	28.01	7.95
2626	1928	27.42	8.29
2629	2050	28.00	7.96
2631	2113	29.60	8.16
2632	2100	28.23	7.84
2698	2008	26.83	7.80
2702	2050	28.07	8.00
2760	2047	28.00	8.01
2760	2036	27.20	7.82
2772	2045	27.91	7.99

[a] Standard uncertainty u(p) = 4 kPa and the combined expanded relative uncertainties $U_r(T) = 0.7\%$, $U_r(c_P) = 15.2\%$, $U_r(k) = 19.4\%$, $U_r(\alpha) = 15.0\%$ with 0.95 level of confidence (coverage factor of 2).

Table 7
Summary of parameters used in the specific heat capacity and thermal conductivity models.

Parameter description	Units	Symbol	Value	Reference
Debye temperature in "a" direction	K	ϑ_a	2280	[73]
Debye temperature in "c" direction	K	ϑ_c	760	[73]
Sommerfeld constant	mJ mol^{-1} K^{-2}	γ_e	0.014	[74]
formation enthalpy of Frenkel pair	kJ	ΔH_F	467.94	[75]
bulk modulus	GPa	K_T	8.82	[76]
Lorenz number	μW Ω K^{-2}	L	200	[77]
Grüneisen parameter	–	γ	2.0	[78]
atomic mass	u	M_{at}	12.01	[79]
free electrons per carbon atom	–	n_e	1.0	[80]
deformation potential	ev	ε_1	6.13	[81]
grain size	μm	L_g	7.0	[82]
thermal conductivity of pore gas	W m^{-1} K^{-1}	k_p	0.07	[70]
pore fraction (at 298 K)	–	v_p	0.202	*
molar mass	kg mol^{-1}	M_{mol}	0.012	–
atomic volume	Å^3	Ω	8.813	–
density (theoretical)	kg m^{-3}	ρ_{TD}	2260	[83]

* experimentally determined from the measured density (ρ_{298}) and theoretical density (ρ_{TD}).
[a] Standard uncertainty u(v_p) = 0.002.

4. Discussion: Comparison with solid state theory

4.1. Specific heat capacity

In order to understand the evolution of specific heat capacity, as a function of temperature, it is necessary to deconvolute the various contributing mechanisms. One can express the specific heat in the following way:

$$c_P^{tot} = c_V^h + c_V^{el} + c_V^d + c_V^m + \Delta c_{V\to P} \tag{19}$$

where the superscripts "h", "el", "d" and "m" stand for harmonic, electronic, defect and magnetic contributions, respectively and the subscript "V" means at constant volume. Detailed analysis of the

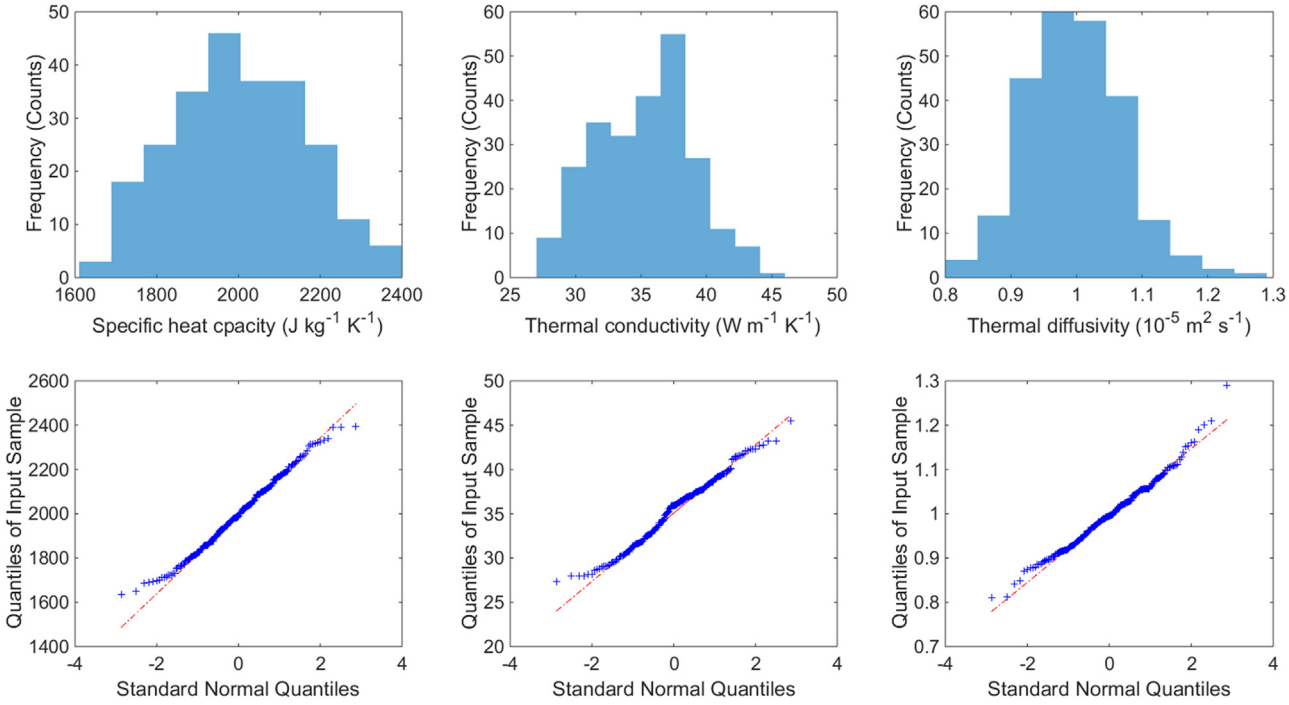


Fig. 13. Histogram of specific heat values (top left) with its respective quantile – quantile plot (bottom left), thermal conductivity values (top middle) with its respective quantile – quantile plot (bottom middle) and thermal diffusivity values (top right) with its respective quantile – quantile plot (bottom right).

individual mechanisms (refer to Appendix A and Table 7) lead to Eq. (20):

$$c_v^{tot} = 9N_A C_B \left(\frac{T}{\vartheta}\right)^3 \int_0^{\frac{\vartheta_l}{T}} \frac{x^4 e^x}{(e^x-1)^2} dx + \gamma_e T + \frac{\sqrt{6}\Delta H_F{}^2}{2RT^2} exp\left(-\frac{\Delta H_F}{2RT}\right) + \frac{\alpha^2 T K_T M_{mol}}{\rho(T)} \quad (20)$$

It must be noted that second order and higher anharmonic contributions are not treated by Eq. (20).

From Fig. 10 it is evident that there is excellent agreement between the model and both the current and previous experimental data. The model therefore demonstrates the current experimental results can be understood in terms of established physics. At high temperatures the specific heat capacity saturates and approaches the Dulong-Petit limit. This occurs as a result of a decrease in the number of new, higher energy, unoccupied phonon states. The slight linear ascent noticeable above 2300 K results from the small electronic contribution to C_p. A significant defect contribution towards specific heat capacity would only be expected at temperatures above 3500 K due to the large formation energies associated with the creation of Frenkel pairs.

4.2. Thermal conductivity

Graphite is a semi-metal, meaning its Fermi level lies in the conduction band, just above the band edge. Thus, conduction electrons, as well as phonons, contribute to thermal transport. Thus, the thermal conductivity can be written as [72]:

$$k_{tot} = k_{el} + k_l \quad (21)$$

where k_{el} and k_l stand for the electronic and lattice contribution respectively.

The model described in Appendix B is presented in Fig. 11 and all input parameters are listed in Table 7. It is clear that the model is in very good agreement with experimental data. The observed maximum, which occurs close to 300 K, is due to the competition between two main mechanisms: 1) phonon heat capacity appreciation and 2) phonon life time reduction. From 0 K to 300 K the thermal conductivity increases as it is dominated by the increase in the phonon specific heat. Above 300 K this increase is overcome by degradation of thermal conductivity due to an increase in the frequency of phonon scattering events. This diminishes the average phonon life time. At temperatures below 300 K phonon scattering is dominated by electron- phonon interactions, grain boundary scattering and impurity scattering, while at higher temperatures phonon–phonon interactions become the dominant scattering mechanism. The overall agreement between theory, new and previous experimental data supports the efficacy of the experimental approach presented here.

4.3. Error analysis

Previously little effort has been made to accurately estimate the error of equivalent methods (arising from uncertainty in input parameters) [17,84]. The sensitivity analysis performed (shown in Fig. 5) has shown that the five input parameters – total hemispherical emissivity, spatial laser profile, absorptivity thickness and density, have a significant impact on the calculated thermogram. These parameters are then used as factors in a 3-level full factorial design.

The five parameters selected, based on the sensitivity study, have been split into three levels corresponding to a best estimate, minimum and maximum value, both at two standard deviations away from the mean estimated value. The corresponding histograms of the output are presented in Fig. 13. From the quantile-quantile plots it can be seen that a normal distribution is a reasonable approximation of the output distributions of thermal conductivity, specific heat capacity and thermal diffusivity.

Assuming the input parameters are randomly distributed and treating them as independent events, the total uncertainty can be represented in the following way:

$$\sigma_{total} = \sigma_{model} + \sigma_{exp.} \quad (22)$$

where $\sigma_{exp.}$ is the uncertainty associated with experimental scatter based on a variation in the recorded thermograms for the same measurement temperature, while σ_{model} is the propagated error resulting from uncertainties in the five model input parameters – total hemispherical emissivity, spatial laser profile, absorptivity (spectral emissivity at 1064 nm), density and thickness. The number of different ways to combine the 5 input parameters, each consisting of 3 levels, is 243. One can weigh the output of each combination of input parameters assuming a Gaussian probability density function for each input parameter.

$$\sigma_{model} = \sqrt{\sum_{k=1}^{243} \frac{w_k \left(y_k - \overline{y_w}\right)^2}{\left(\frac{N}{N-1}\sum w_k\right)}} \tag{23}$$

where k is the combination index, y_k is the output value (α, C_P, k) of that particular combination and the weighted mean ($\overline{y_w}$) is:

$$\overline{y_w} = \frac{\sum_{k=1}^{243} y_k w_k}{\sum_{k=1}^{243} w_k} \tag{24}$$

where the weight (w_k) is expressed as follows:

$$w_k = \prod_{i=1}^{5} \left[exp \frac{-\left(x_{ij} - \mu_i\right)^2}{2{\sigma_i}^2} \right] \tag{25}$$

where the value of a certain parameter of certain level is:

$$x_{ij} = \begin{cases} \mu_i + 2\sigma_i for j = 1 \\ \mu_i for j = 2 \\ \mu_i - 2\sigma_i for j = 3 \end{cases} \tag{26}$$

where μ represents the arithmetic mean, σ stands for one standard deviation, i represents the input parameter and j is the level.

The results from the error analysis are summarized in Table 8. Thermal conductivity has the largest associated error of 20% while specific heat capacity and thermal diffusivity have an error of around 15%. The reason for thermal diffusivity having a smaller associated error is due to the negative correlation between thermal conductivity and specific heat capacity, whereby the increase in the fitted value of one of these properties is generally compensated by an increase in the other. This implies that thermal diffusivity, representing the ratio of the two prior properties, would not necessarily follow the error propagation law, as seen from Table 8.

5. Conclusions

This paper has presented a new numerical inverse method and improved apparatus for the determination of high temperature thermo-physical properties of materials. Specifically:

- A significant improvement in the accuracy of how the laser spatial profile is implemented in the FEA model is shown to improve the evaluation of thermal conductivity and specific heat capacity by 15% and 20%, respectively.
- The apparatus has been modified for the simultaneous measurement of spectral emissivity, reducing the uncertainty in the measured temperature to 0.3–0.7% between 1500 and 3000 K. Other strengths include high temperature capability, simultaneous property evaluation and semi-empirical determination of the convective heat transfer coefficient instead of fitting.
- The method has been tested on isotropic graphite and specific heat capacity, thermal conductivity and thermal diffusivity are in good agreement with literature values.
- The measured temperature range of these properties for isotropic, isostatically pressed graphite has been extended from 1700 K to 2800 K.
- The errors in specific heat capacity and thermal diffusivity values have been estimated to be 15% while the error in thermal conductivity approaches 20%.
- A model based on the Klemens and Debye formalism has been proposed for the temperature evolution of specific heat capacity, thermal conductivity and thermal diffusivity of isotropic graphite.
- The values obtained from the model are in very good agreement with previous experimental data and the new experimental data up to 2800 K. This provides additional confidence in the experimental approach presented here.

Table 8
Summary of the output uncertainty of specific heat (Δc_P), thermal conductivity (Δk) and thermal diffusivity ($\Delta\alpha$) for a thermogram at temperature T = 2050 K and at a pressure p = 0.4 MPa.

uncertainty type	Δc_P (J kg^{-1} K^{-1})	Δk (W m^{-1} K^{-1})	$\Delta\alpha$ (10^{-6} m^2 s^{-1})
$2\sigma_{model}/\overline{y_w}$	0.095	0.123	0.085
$2\sigma_{exp.}/\overline{y_w}$	0.047	0.071	0.065
$2\sigma_{total}/\overline{y_w}$	0.152	0.194	0.150

[a] Standard uncertainty u(p) = 4 kPa and the combined expanded relative uncertainty $U_r(T)$ = 0.7% with 0.95 level of confidence (coverage factor of 2).

Acknowledgements

Thanks are due to Davide Robba for assistance in the lab. Konstantinos Boboridis is thanked for fruitful discussions and expert advice on problems related to optics and radiation thermometry. Finally, the European Commission is thanked for the funding provided to support the current work.

Appendix A. Model of specific heat

The harmonic contribution to specific heat capacity was calculated using the Debye approach, where lattice vibrations are treated as phonons in a box with wavelengths varying from two times the inter-atomic spacing up to the dimensions of the box. Debye expressed the specific heat capacity in the following way:

$$c_V^h = 9N_A C_B \left(\frac{T}{\vartheta}\right)^3 \int_0^{\frac{\vartheta}{T}} \frac{x^4 e^x}{\left(e^x - 1\right)^2} dx \tag{A 1}$$

The evaluation of this integral can be performed numerically using the trapezium rule.

The hexagonal crystal structure of graphite imposes a degree of anisotropy on the thermal transport. The macroscopic isotropy is achieved by small, randomly oriented grains. Nevertheless, on the meso-scale there are two major contributions – from in-plane and out-of plane vibrations. Hence, the harmonic term of the specific heat capacity can be described in the following way [73]:

$$c_V^h = \frac{2}{3} c_v^{h_a} + \frac{1}{3} c_v^{h_c} \tag{A 2}$$

$$c_V^h = 9N_A C_B \left(\frac{T}{\vartheta_i}\right)^3 \int_0^{\frac{\vartheta_i}{T}} \frac{{x_i}^4 e^{x_i}}{\left(e^{x_i} - 1\right)^2} dx_i \tag{A 3}$$

$$x_i = \frac{\hbar\omega_i}{C_B T_i} \tag{A 4}$$

where i = a or c stand for contributions from the crystallographic directions along the a-axis and c-axis respectively, C_B is Boltzmann's constant (m^2 kg s^{-2} K^{-1}), ω is the phonon frequency, T is temperature (K), ϑ is the Debye temperature (K) and N_A is the number of atoms per mole (mol^{-1}). There is some uncertainty in the

reported values for in-plane and out of plane Debye temperatures [85]: here the values have been taken from Magnus [73] as 2280 K and 760 K respectively.

The electronic contribution can be approximated by the following equation [74]:

$$c_V^{el} = \gamma_e T \tag{A 5}$$

where γ_e is the Sommerfield coefficient.

The specific heat capacity contribution due to defect formation can be derived from statistical thermodynamics. Assuming that the dominant defect species will be Frenkel pairs and based on the work by Reich et al. [75] it is estimated that there are 6 interstitial sites per carbon atom. This leads to the following expression for configurational entropy:

$$\Delta S_{conf} = Rln\left(\Omega\right) \tag{A 6}$$

$$(A7)\Omega = W_i W_v$$

$$\Omega = \frac{(6N)!}{(6N-n)!n!} \times \frac{(N)!}{(N-n)!n!} \tag{A 8}$$

where R is the gas constant, N is the number of carbon lattice sites and n is the number of vacancies. Using Stirling's approximation [86] (Eq. (A 6)) for high values of N:

$$\ln(N!) \sim Nln(N) - N \tag{A 9}$$

$$\frac{d\Delta S_{conf}}{dn} = \ln\left(\frac{n^2}{(1-n)(6-n)}\right) \tag{A 10}$$

The total contribution to the enthalpy can be expressed as:

$$(A11)\Delta H = n\Delta H_F$$

where ΔH_F is the enthalpy of formation for a carbon Frenkel pair. At equilibrium $\frac{d\Delta G}{dn} = 0$ and assuming negligible contributions from the vibrational entropy term the following expression holds:

$$\Delta H_F = RT\frac{d\Delta S_{conf}}{dn} \tag{A 12}$$

$$n = \sqrt{(1-n)(6-n)}exp\left(-\frac{\Delta H_F}{2RT}\right) \tag{A 13}$$

Assuming small defect concentrations:

$$n = \sqrt{6}exp\left(-\frac{\Delta H_F}{2RT}\right) \tag{A 14}$$

Hence

$$c_V^d = \frac{d(n\Delta H_F)}{dT} = \frac{\sqrt{6}{\Delta H_F}^2}{2RT^2}exp\left(-\frac{\Delta H_F}{2RT}\right) \tag{A 15}$$

Finally, considering polycrystalline graphite is diamagnetic and has no unpaired electrons one can assume its net magnetization is equal to zero and thus:

$$c_V^m = 0 \tag{A 16}$$

In order to convert the specific heat at constant volume to one at constant pressure the following expression has been used, which takes into account the quasi-harmonic contribution of thermal expansion to specific heat capacity:

$$c_p = c_V + \frac{\alpha^2 TK_T M_{mol}}{\rho(T)} \tag{A 17}$$

$$\Delta c_{V\to P} = c_p - c_V = \frac{\alpha^2 TK_T M_{mol}}{\rho(T)} \tag{A 18}$$

where K_T (Pa) is the bulk modulus at constant temperature, α is the linear thermal expansion coefficient ($m\,K^{-1}$), M_{mol} is the molar mass ($kg\,mol^{-1}$) and $\rho(T)$ is the temperature dependent density ($kg\,m^{-3}$).

$$c_v^{tot} = 9N_A C_B\left(\frac{T}{\vartheta}\right)^3 \int_0^{\frac{\vartheta_i}{T}} \frac{x^4 e^x}{(e^x-1)^2}dx + \gamma_e T + \frac{\sqrt{6}{\Delta H_F}^2}{2RT^2}$$
$$exp\left(-\frac{\Delta H_F}{2RT}\right) + \frac{\alpha^2 TK_T M_{mol}}{\rho(T)} \tag{A 19}$$

It must be noted that second order and higher anharmonic contributions are not treated.

Appendix B. Model of thermal conductivity

The electronic contribution (k_{el}) to thermal conductivity is treated semi-empirically. According to the Wiedmann-Franz law [72] one can express the electronic term as:

$$k_{el} = L\sigma(T)T = \frac{LT}{\Upsilon(T)} \tag{B 1}$$

where T is temperature (K), L is the Lorenz number ($W\,\Omega\,K^{-2}$), σ is the electrical conductivity ($\Omega^{-1}\,m^{-1}$) and Υ is the electrical resistivity ($\Omega\,m$). The resistivity is taken from literature data on isotropic polycrystalline graphite [87] and the following expression has been fit to the data:

$$\Upsilon(T) = \begin{cases} -3.91\times10^{-7}T^3 + 1.65\times10^{-3}T^2 \\ -2.15\times T + 1.75\times10^3 \in T < 1700K \\ 2.15\times10^{-1}T + 5.56\times10^2 \in T > 1700K \end{cases} \tag{B 2}$$

The theoretical Lorenz number is $2.443\times10^{-8}\,W\,\Omega\,K^{-2}$, however, lower values have been determined experimentally [77,88]. In this work the value of $2.0\times10^{-8}\,W\,\Omega\,K^{-2}$ was used based on the work by Bapat et al. [77]

With the effective medium approach of Bruggeman [89] one can express the lattice thermal conductivity of a polycrystalline material with polyhedral grains as follows:

$$k_l = \frac{1}{2}\left(-k_c + \left({k_a}^2 + 8k_c k_a\right)^{\frac{1}{2}}\right) \tag{B 3}$$

where the subscripts "a" and "c" stand for the respective crystallographic directions.

$$k_i = \left(\frac{C_B}{\hbar}\right)^3 \frac{C_B}{2\pi^2 V_i}T^3 \int_0^{\frac{\vartheta_i}{T}} \frac{\tau_{tot}{x_i}^4 e^{x_i}}{(e^{x_i}-1)^2}dx_i \tag{B 4}$$

where i is the index of the respective crystallographic direction ($i = a$ or c), V_i is the sound velocity in graphite in the direction i ($m\,s^{-1}$), and τ_{tot} is the total relaxation time (s), which can be expressed as follows:

$$\frac{1}{\tau_{tot}} = \frac{1}{\tau_u} + \frac{1}{\tau_{im}} + \frac{1}{\tau_{gb}} + \frac{1}{\tau_{e-ph}} \tag{B 5}$$

where $\tau_u$represents the contribution from Umklapp processes and according to the work by Klemens [78] can be expressed as follows:

$$\frac{1}{\tau_u} = \frac{2\gamma^2 C_B T\omega^2}{MV_i\omega_i^d} \tag{B 6}$$

where γ is the Grüneisen parameter, M is the atomic mass and ω_i^d is the Debye frequency. Furthermore, since graphite contains around 1% C^{13} the following impurity scattering mechanism can be employed[90]:

$$\frac{1}{\tau_{im}} = \left(\frac{\Delta M}{M}\right)^2 \frac{n_{im}{C_B}^4\Omega\omega^4}{4\pi\hbar^4 V_i} \tag{B 7}$$

where ΔM is the impurity atom-host atom mass difference and n_{im} is the concentration of impurity atoms and Ω is the atomic volume.

Since, this type of graphite is fine grained with a specified grain size of 7 μm, one can express a purely diffuse scattering due to grain boundaries using the following expression[90]:

$$\frac{1}{\tau_{gb}} = \frac{V_i}{L_g} \quad \text{(B 8)}$$

where L_g is the mean free path due to boundary scattering and is approximately equal to the grain size. Finally, graphite is a semi-metal and hence there will be interaction between the free conduction electrons and the lattice phonons, which is expressed in the following way [91]:

$$\frac{1}{\tau_{e-ph}} = \frac{n_e {\varepsilon_1}^2 \omega}{\rho_{TD} {V_i}^2 C_B T} \sqrt{\frac{\pi m^* V_i}{2C_B T}} exp\left(-\frac{m^* {V_i}^2}{2C_B T}\right) \quad \text{(B 9)}$$

where n_e is the free electron number density, ε_1 is the deformation potential, m^* is the effective electron mass and ρ_{TD} is the material theoretical density.

The above formulation of thermal conductivity applies to fully dense graphite (k_s) and since thermal conductivity is dependent on porosity, an appropriate correction must be made. As a result the experimental data could then be compared to the results obtained from the phonon scattering model described above. The following correction has been applied according to "Effective medium percolation theory" [92]:

$$k_{eff} = \frac{1}{4}\left[k_p\left(3v_p - 1\right) + k_s\left(3v_s - 1\right) + \left(\left(k_p\left(3v_p - 1\right) + k_s\left(3v_s - 1\right)\right)^2 + 8k_p k_s\right)^{\frac{1}{2}}\right] \quad \text{(B 10)}$$

where k_{eff}, k_s and k_p are the effective, solid and pore thermal conductivities while v_p and v_s stand for pore and solid volume fractions.

References

[1] A.O. Desjarlais, R.R. Zarr, Design concepts for a new guarded hot plate apparatus for use over an extended temperature range, Mater. Test. Appl. (2002) 98–101.
[2] S. André, B. Rémy, F. Pereira, Hot wire method for the thermal characterization of materials: inverse problem application, Eng. Termica. 4 (2003) 55–64.
[3] H. Roder, R. Perkins, Absolute steady-state thermal conductivity measurements by use of a transient hot-wire system, J. Res. Natl. Inst. Stand. Technol. 105 (2000) 221–253 (Accessed 14 September 2015) http://nvlpubs.nist.gov/nistpubs/jres/105/2/j52rod.pdf.
[4] H.-J. Höhne, G.W.H. Hemminger, W.F. Flemmersheim, Differential scanning calorimetry, Anal. Bioanal. Chem. (2004) 366–367, http://dx.doi.org/10.1007/s00216-004-2814-8.
[5] A. Leadbetter, Anharmonic effects in the thermodynamic properties of solids I. An adiabatic calorimeter for the temperature range 25–500 °C: the heat capacities of Al2O3, Al and Pb, J. Phys. C Solid State Phys. 1 (1968) 1481–1488 (Accessed 15 September 2015) http://iopscience.iop.org/0022-3719/1/6/304.
[6] E. West, D. Ginnings, An adiabatic calorimeter for the range 30 to 500C, J. Res. Natl. Bur. Stand. 60 (1958) (1934) 309–316 (Accessed 15 September 2015) http://nvlpubs.nist.gov/nistpubs/jres/60/jresv60n4p309_A1b.pdf.
[7] F. Kohlrausch, On the stationary temperature state of a conductor heated by an electric current, Berlin Akad. 38 (1899) 711–718.
[8] Z. Zeng, C. Shen, B. Shen, Z. Hu, Cross-plane thermal conductivity and thermal diffusivity measurement in thin-films by one-dimensional thermal wave method, IEEE Int. Conf. Nano/Micro Eng. Mol. Syst. (2011) 1080–1084.
[9] W.J. Parker, R.J. Jenkins, C.P. Butler, G.L. Abbott, Flash method of determining thermal diffusivity, heat Capacity, and thermal conductivity, J. Appl. Phys. 32 (1961) 1679–1684, http://dx.doi.org/10.1063/1.1728417.
[10] A. Seifter, K. Boboridis, A. Obst, Comparison of emissivity measurements using an integrating sphere reflectometer and a laser polarimeter on surfaces with various degrees of roughness, Proc. XVIII MEKO World Congr. (2013) 1623–1628 (Accessed 3 December 2015) http://www.imeko.org/publications/wc-2003/PWC-2003-TC12-009. pdf.
[11] D. Partouche-Sebban, J. Pelissier, Emissivity and temperature measurements under shock loading, along the melting curve of bismuth, Shock Waves 12 (2003) 69–81, http://dx.doi.org/10.1007/s00193-003-0192-3 (Accessed 4 December 2015).
[12] P. Coates, Multi-wavelength pyrometry, Metrologia 17 (1981) 103–109 (Accessed 10 September 2015) http://iopscience.iop.org/0026-1394/17/3/006.
[13] P.C. Burns, R.C. Ewing, A. Navrotsky, Nuclear fuel in a reactor accident, Science 80 (335) (2012) 1184–1188, http://dx.doi.org/10.1126/science.1211285.
[14] M.J. Gash, D.T. Ellerby, S.M. Johnson, Ultra high temperature ceramic composites, Handb. Ceram. Compos (2005) 197–223, http://dx.doi.org/10.1017/CBO9781107415324.004.
[15] L.S. Walker, Processing of Ultra High Temperature Ceramics, 2012.
[16] R.D. Cowan, Pulse method of measuring thermal diffusivity at high temperatures, J. Appl. Phys. 34 (1963) 926–927, http://dx.doi.org/10.1063/1.1729564.
[17] C. Ronchi, W. Heinz, M. Musella, R. Selfslag, M. Sheindlin, A universal laser-pulse apparatus for thermophysical measurements in refractory materials at very high temperatures, Int. J. Thermophys. 20 (1999) 987–996.
[18] T. Baba, A. Ono, Improvement of the laser flash method to reduce uncertainty in thermal diffusivity measurements, Meas. Sci. Technol. 12 (2001) 2046–2057, http://dx.doi.org/10.1088/0957-0233/12/12/304.
[19] M. Musella, Development and Test of a Method for the Simultaneous Measurement of Heat Capacity and Thermal Diffusivity by Laser-flash Technique at Very High Temperatures: Application to Uranium Dioxide, 1999 http://webcat.warwick.ac.uk/record=b1368728?S9.
[20] W.M. Flynn, High-Temperature Guarded Hot Plate Apparatus – Control of Edge Heat Loss, 2005.
[21] C.F. Gilbo, The use of envelope type cold plates in thermal conductivity apparatus, Symp. Therm. Conduct. Meas. Appl. Therm. Insul. (1957) 18–31.
[22] J.R. Parsons, J.C. Mulligan, Measurement of the properties of liquids and gases using a transient hot-wire technique, Rev. Sci. Instrum. 49 (1978) 1460–1463, http://dx.doi.org/10.1063/1.1135287.
[23] R. Coquard, D. Baillis, D. Quenard, Experimental and theoretical study of the hot-wire method applied to low-density thermal insulators, Int. J. Heat Mass Transf. 49 (2006) 4511–4524, http://dx.doi.org/10.1016/j.ijheatmasstransfer.2006.05.016.
[24] H. Ziebland, J. Burton, The thermal conductivity of liquid and gaseous oxygen, Br. J. Appl. Phys. 6 (1955) 416–420 (Accessed 14 September 2015) http://iopscience.iop.org/0508-3443/6/12/302.
[25] B. Fox, J.L. Rempe, D.L. Knudson, K.G. Condie, In-Pile Thermal Conductivity Measurement Method for Nuclear Fuels Thermal Expansion Symposium, 2009.
[26] N.S. Rasor, J.D. McClelland, Thermal property measurements at very high temperatures, Rev. Sci. Instrum. 31 (1960) 595–604, http://dx.doi.org/10.1063/1.1931263.
[27] T. Czichos, Handbook of Materials Measurement Methods, Springer Science + Business Media, Inc., 2006, 2017.
[28] A. Smith, N. Rasor, Observed dependence of the low-temperature thermal and electrical conductivity of graphite on temperature, type, neutron irradiation, and bromination, Phys. Rev. 104 (1956) 885–891, http://dx.doi.org/10.1002/cbdv.200490137/abstract.
[29] K. Boboridis, Thermophysical property measurements on niobium and titanium by a microsecond-resolution pulse-heating technique using high-speed laser polarimetry and, Int. J. Thermophys. 23 (2002) 277–291, http://dx.doi.org/10.1023/A:1013977732267 (Accessed 15 September 2015).
[30] P. Flubacher, A low temperature adiabatic calorimeter for condensed substances. Thermodynamic properties of argon, Proc. Phys. Soc. 78 (1961) 1449–1461 (Accessed 15 September 2015) http://iopscience.iop.org/0370-1328/78/6/346.
[31] Z. Tan, G. Sun, Y. Sun, A. Yin, W. Wang, An adiabatic low-temperature calorimeter for heat capacity measurement of small samples, J. Therm. Anal. 45 (1995) 59–67, http://dx.doi.org/10.1007/BF02548664 (Accessed 15 September 2015).
[32] L. Leibowitz, Enthalpy of solid uranium dioxidefrom 2500 K to its melting point, J. Nucl. Mater. 29 (1969) 356–358 (Accessed 29 January 2016) http://scholar.google.com/scholar?hl=en&btnG=Search&q=intitle:ENTHALPY+OF+SOLID+URANIUM+DIOXIDE+FROM+2500+K+TO+ITS+MELTING+POINT#0.
[33] D. Fischer, L. Leibowitz, M. Chasanov, A High- Temperature Calorimeter System for Use with Materials Containing Plutonium, 1971 (Accessed 29 January 2016) http://www.osti.gov/scitech/biblio/4683123.
[34] O. Beneš, Thermodynamics of Molten Salts for Nuclear Applications, 2008.
[35] O. Beneš, R.J.M. Konings, C. Kuenzel, M. Sierig, A. Dockendorf, L. Vlahovic, The high-temperature heat capacity of the (Li, Na)F liquid solution, J. Chem. Thermodyn. 41 (2009) 899–903, http://dx.doi.org/10.1016/j.jct.2009.02.009.
[36] K. Bakker, H. Hein, Thermophysical property measurements and ion-implantation studies on CePO 4, J. Nucl. Mater. 252 (1998) 228–234 (Accessed 15 September 2015) http://www.sciencedirect.com/science/article/pii/S0022311597003000.
[37] R.L. Gibby, L. Leibowitz, J.F. Kerrisk, D.G. Clifton, Analytical expressions for enthalpy and heat capacity for uranium-plutonium oxide, J. Nucl. Mater. 50 (1974) 155–161, http://dx.doi.org/10.1016/0022-3115(74)90152-4.
[38] S.C. Mraw, Mathematical treatment of heat flow in differential scanning calorimetry and differential thermal analysis instruments, Rev. Sci. Instrum. 53 (1982) 228–231, http://dx.doi.org/10.1063/1.1136933.
[39] E. Capelli, O. Beneš, R.J.M. Konings, Excess heat capacity of the (Li1-xCax)F1 + x liquid solution determined by differential scanning calorimetry and drop calorimetry, J. Chem. Thermodyn. 81 (2015) 160–166, http://dx.doi.org/10.1016/j.jct.2014.10.007.
[40] R.L. Danley, New heat flux DSC measurement technique, Thermochim. Acta 395 (2003) 201–208, http://dx.doi.org/10.1016/S0040-6031(02)00212-5.

[41] B. Hay, J. Hameury, N. Fleurence, P. Lacipiere, M. Grelard, V. Scoarnec, G. Davee, New facilities for the measurements of high-temperature thermophysical properties at LNE, Int. J. Thermophys. 35 (2013) 1712–1724, http://dx.doi.org/10.1007/s10765-013-1400-8.
[42] H.W. Baxter, Determination of specific heat of metals, Nature 153 (1944) 316.
[43] C. Affrotit, Contribution à l'étude Des Chaleurs Specifiques Des Composes d'actinides [Contribution to the Study of Specific Heats of Actinide Compounds], 1970.
[44] A.M. Nathan, A dynamic method for measuring the specific heat of metals, J. Appl. Phys. 22 (1951) 234, http://dx.doi.org/10.1063/1.1699933.
[45] J. Cape, G. Lehman, Temperature and finite pulse time effects in the flash method for measuring thermal diffusivity, J. Appl. Phys. 34 (1963) 1909–1913, http://dx.doi.org/10.1063/1.1729711.
[46] T. Baba, M. Kobayashi, A. Ono, J.H. Hong, M.M. Suliyanti, Experimental investigation of the nonuniform heating effect in laser flash thermal diffusivity measurements, Thermochim. Acta 218 (1993) 329–339, http://dx.doi.org/10.1016/0040-6031(93)80433-B.
[47] R.D. Cowan, Proposed method of measuring thermal diffusivity at high temperatures, J. Appl. Phys. 32 (1961) 1363–1370, http://dx.doi.org/10.1063/1.1736235.
[48] M. Sheindlin, D. Halton, M. Musella, C. Ronchi, Advances in the use of laser-flash techniques for thermal diffusivity measurement, Rev. Sci. Instrum. 69 (1998) 1426, http://dx.doi.org/10.1063/1.1148776.
[49] A. Kaźmierczak-Bałata, Determination of thermal-diffusivity dependence on temperature of transparent samples by thermal wave method, Int. J. Thermophys. 31 (2010) 180–186, http://dx.doi.org/10.1007/s10765-009-0676-1.
[50] L. Filippov, Periodic heating methods in thermophysical experiments, Meas. Tech 5 (1980) 431–434 (Accessed 4 September 2015) http://www.springerlink.com/index/x72qq640jx3u276w.pdf.
[51] J.A. Malen, K. Baheti, T. Tong, Y. Zhao, J.A. Hudgings, A. Majumdar, Optical measurement of thermal conductivity using fiber aligned frequency domain thermoreflectance, J. Heat Transf. 133 (2011) 1–7, http://dx.doi.org/10.1115/1.4003545.
[52] J. Morikawa, T. Hashimoto, A. Maesono, Simultaneous measurement of thermal diffusivity, heat capacity, and thermal conductivity by Fourier transform thermal analysis, High Temp. Press. 33 (2001) 387–395, http://dx.doi.org/10.1068/htwu377.
[53] P.A. Ni, R.M. More, H. Yoneda, F.M. Bieniosek, Polarization pyrometry: an improvement to multi-wavelength optical pyrometry, Rev. Sci. Instrum. 83 (2012) 123501, http://dx.doi.org/10.1063/1.4768473.
[54] A. Cezairliyan, S. Krishanan, J. McClure, Simultaneous measurements of normal spectral emissivity by spectral radiometry and laser polarimetry at high temperatures in millisecond-resolution pulse-heating experiments: application to molybdenum and tungsten, Int. J. Thermophys. 17 (1996) 1455–1473, http://dx.doi.org/10.1007/BF01438679 (Accessed 15 September 2015).
[55] A. Seifter, K. Boboridis, A. Obst, Emissivity measurements on metallic surfaces with various degrees of roughness: a comparison of laser polarimetry and integrating sphere reflectometry, Int. J. Thermophys. 25 (2004) 547–560, http://dx.doi.org/10.1023/B:IJOT.0000028489.81327.b7 (Accessed 2 December 2015).
[56] W. Finkel, Integration sphere theory, Opt. Commun. 2 (1970) 25–28.
[57] D.I. Milburn, K.G.T. Hollands, The directional response error in integrating-sphere transmittance measurements at solar wavelength, Solar Energy 55 (1995) 85–91.
[58] J. Gardner, T. Jones, Multi-wavelength radiation pyrometry where reflectance is measured to estimate emissivity, J. Phys. E 306 (1980) 306–310 (Accessed 15 September) http://iopscience.iop.org/0022-3735/13/3/016.
[59] B. Hay, K. Anhalt, L. Chapman, K. Boboridis, High temperature thermophysical properties of advanced materials for nuclear design, 2nd IMEKO TC 11 Int Symp. Metrol. Infrastruct. (2011).
[60] PDE Solutions, FlexPDE, 2013.
[61] B. Hay, K. Anhalt, L. Chapman, K. Boboridis, J. Hameury, S. Krenek, L. Vlahovic, N. Fleurence, O. Beneš, Traceability improvement of high temperature thermal property measurements of materials for new fission reactors, IEEE Trans. Nucl. Sci. 61 (2014) 2112–2119 (Accessed 15 November 2015) http://ieeexplore.ieee.org/xpls/abs_all.jsp?arnumber=6759752.
[62] T. Matsumoto, A. Ono, Specific heat capacity and emissivity measurements of ribbon-shaped graphite using pulse current heating, Int. J. Thermophys. 16–16 (1995) 267–275, http://dx.doi.org/10.1007/BF01438977.
[63] D. Marquardt, An algorithm for least-squares estimation of nonlinear parameters, J. Soc. Ind. Appl. Math. 11 (1963) 431–441, http://dx.doi.org/10.1137/0111030 (Accessed 13 January 2016).
[64] J. Moore, The levenberg marquardt method implementation and theory, Conf. Numevical Anatysis (1977) 1–12.
[65] C. Ronchi, M. Sheindlin, Thermal conductivity of uranium dioxide up to 2900 K from simultaneous measurement of the heat capacity and thermal diffusivity, J. Appl. Phys. 85 (1999) 776–789, http://dx.doi.org/10.1063/1.369159 (Accessed 15 September 2015).
[66] A. Salazar, A. Mendioroz, Extending the flash method to measure the thermal diffusivity of semitransparent solids, Meas. Sci. Technol. 25 (2014) 1–7, http://dx.doi.org/10.1088/0957-0233/25/3/035604.
[67] M. Sheindlin, D. Staicu, C. Ronchi, L. Game-Arnaud, B. Remy, A. Degiovanni, Experimental determination of the thermal conductivity of liquid UO2 near the melting point, J. Appl. Phys. 101 (2007), http://dx.doi.org/10.1063/1.2721091.
[68] J. Lienhard, A Heat Transfer Textbook, 3rd ed., 2013.
[69] W. Little, Tables of Thermodynamic Properties of Argon from 100 to 3000 K, 1964.
[70] R.B. Stewart, R.T. Jacobsen, Thermodynamic properties of argon from the triple point to 1200 K with pressures to 1000 MPa, J. Phys. Chem. Ref. Data 18 (1989) 639, http://dx.doi.org/10.1063/1.555829.
[71] D.P. DeWitt, G.D. Nutter, Theory and Practice of Radiation Thermometry, 1988.
[72] W. Jones, N.H. March, Theoretical Solid State Physics, 1973.
[73] A. Magnus, Die spezifische Wärme des Kohlenstoffs, Siliziums und Siliziumkarbids bei hohen Temperaturen [The specific heat of carbon, silicon and silicon carbide at high temperatures], Ann. Phys. 375 (1923) 303–331, http://dx.doi.org/10.1002/andp.19233750405/abstract (Accessed 15 January 2016).
[74] G.R. Stewart, Measurement of low-temperature specific heat, Rev. Sci. Instrum. 54 (1983) 1, http://dx.doi.org/10.1063/1.1137207.
[75] L. Li, S. Reich, J. Robertson, Defect energies of graphite: density-functional calculations, Phys. Rev. B 72 (2005) 184109, http://dx.doi.org/10.1103/PhysRevB.72.184109.
[76] J.R. Cost, K.R. Janowski, R.C. Rossi, Elastic properties of isotropic graphite, Philos. Mag. 17 (1968) 851–854, http://dx.doi.org/10.1080/14786436808223035.
[77] S. Bapat, H. Nickel, Thermal conductivity and electrical resistivity of POCO grade AXF-Q1 graphite to 3300 K, Carbon N. Y. 11 (1973) 323–327 (Accessed 14 January 2016) http://www.sciencedirect.com/science/article/pii/0008622373900730.
[78] P.G. Klemens, D.F. Pedraza, Thermal conductivity of graphite basal plane, Carbon N. Y. 32 (2003) 735–741.
[79] M.E. Wieser, T.B. Coplen, Atomic weights of theelements 2009, Pure Appl. Chem. 85 (2013) 1047–1078, http://dx.doi.org/10.1351/PAC-REP-10-09-14.
[80] P.R. Wallace, The band theory of graphite, Phys. Rev. 71 (1947) 622–634, http://dx.doi.org/10.1351/PAC-REP-10-09-14.
[81] J. Heremans, J.P. Michenaud, M. Shayegan, G. Dresselhaus, Magnetisation and deformation potentials in graphite, J. Phys. C Solid State Phys. 14 (1981) 3541–3546, http://dx.doi.org/10.1088/0022-3719/14/24/010.
[82] S. Group, Specialty Graphites for the Photovoltaic Industry, 2015.
[83] C.L. Hoenig, High Density-high Purity Graphite Prepared by Hot Isostatic Pressing in Refractory Metal Containers, 1980.
[84] C. Ronchi, M. Sheindlin, Thermal conductivity of uranium dioxide up to 2900 K from simultaneous measurement of the heat capacity and thermal diffusivity, J. Appl. Phys. 85 (1999) 776–789, http://dx.doi.org/10.1063/1.369159.
[85] W. Morgan, Thermal Expansion Coefficients of Graphite Crystals, 1972.
[86] C.B. Carter, M.G. Norton, Ceramic Materials: Science and Engineering, 2013.
[87] R.E. Taylor, H. Groot, Thermophysical Properties of POCO Graphite, 1978.
[88] S. Bapat, Thermal conductivity and electrical resistivity of two types of ATJ-S graphite to 3500 K, Carbon N. Y. 11 (1973) 511–514 (Accessed 14 January 2016) http://www.sciencedirect.com/science/article/pii/0008622373903102.
[89] V. Bruggeman, Berechnung verschiedener physikalischer Konstanten von heterogenen Substanzen. I. Dielektrizitätskonstanten Substanzen [Calculation of various physical constants of heterogeneous substances. I. dielectri, Ann. Phys. 461 (1935) 665–679, http://dx.doi.org/10.1002/andp.19354160802/abstract (Accessed 19 January 2016).
[90] P. Klemens, The scattering of low-frequency lattice waves by static imperfections, Proc. Phys. Soc. Soc. 69 (1955) 665–679 (Accessed 19 January 2016) http://iopscience.iop.org/0370-1298/68/12/303.
[91] J. Zou, A. Balandin, Phonon heat conduction in a semiconductor nanowire, J. Appl. Phys. 89 (2001) 2932–2938, http://dx.doi.org/10.1063/1.1345515.
[92] B. Nait-Ali, K. Haberko, H. Vesteghem, J. Absi, D.S. Smith, Thermal conductivity of highly porous zirconia, J. Eur. Ceram. Soc. 26 (2006) 3567–3574, http://dx.doi.org/10.1016/j.jeurceramsoc.2005.11.011.